International Forum on Aeroelasticity and Structural Dynamics
IFASD 2024
17-21 June 2024, The Hague, The Netherlands

EXPERIMENTAL INVESTIGATION INTO THE DYNAMIC CHARACTERISTICS OF A TILTING MULTIROTOR SYSTEM

Tanuj Sharma[1], **Djamel Rezgui**[1], **Branislav Titurus**[1]

[1]University of Bristol
School of Civil, Aerospace and Design Engineering
ts17863@bristol.ac.uk
djamel.rezgui@bristol.ac.uk
brano.titurus@bristol.ac.uk

Keywords: eVTOL (Electric Vertical Take-Off and Landing), Experimental Modal Analysis (EMA), Finite Element Analysis (FEA), Sequential Quadratic Programming (SQP), Rotor-structure interaction

Abstract: Urban Air Mobility (UAM) promises a transformative leap in urban transportation, with electric vertical take-off and landing (eVTOL) aircraft at the forefront. Pivotal in eVTOL flexibility, especially during transitional flight phases, are tilting rotors. However, these configurations pose challenges in maintaining dynamic stability and controlling vibration, leading to potential resonance issues during transition phases. This study aims to explore experimentally the dynamic interplay between modal characteristics of a tilting multirotor system with operational parameters such as tilt angle and rotational speed of propellers. The key focus is placed on understanding the system-wide implications induced due to changes in tilt angle and rotor speed. This research particularly focuses on how these operation parameters influence resonance, leading to shift in shifts in modal frequencies and damping variations, which are critical in the design and operation of tilting rotors. To scrutinise these characteristics, a dynamically scaled experimental rig is developed. This multirotor test rig facilitates investigations into how variations in rotor tilt angles and rotor speed impact the system's modal characteristics, including natural frequencies, mode shapes, and damping characteristics. A special emphasis is placed on exploring resonance and its implications under different tilt scenarios and operational speeds. Experimental exploration revealed that natural frequencies decrease with an increase in rotor speed, particularly for higher modes. Whereas, increasing the tilt angle from 0° to 90° results in a substantial increase in frequency and a reduction in amplitude, especially in the first torsional mode. Furthermore, it is found that the system experiences strong resonance at 3120 RPM, where the second-out-plane bending mode is excited by the first rotor harmonics.

NOMENCLATURE

Symbol	Description
E	Young's modulus
ρ	Density of the material
A	Cross-sectional area
W, H	Width and height of the H-cross-section
I_{yy}, I_{zz}	Moment of inertia about the y and z-axis
J	Torsional constant of H-shaped crossection
t_1, t_2	Thickness of the flange and web in H-shaped cross-section
$t_{1\,min}$, $t_{2\,min}$	Minimum thickness of the flange and web
t	Thickness of the rectangular tube arm
L_{beam}	Length of the beam
m_{arm}	Mass of the arm
m_{rotor}	Mass of the rotor assembly
L_{arm}	Length of the arm
x_{rotor}	Spanwise location of the rotor
y_{rotor}, z_{rotor}	Transversal location of the rotor in the z and y-direction
$f_{\text{target mode}}$	Target mode frequency
$f_{\text{target freq}}$	Target frequency
Ω	Angular velocity (RPM)
k_e	Element stiffness matrix
m_e	Element stiffness matrix
K_{global}	Global stiffness matrix
M_{global}	Global mass matrix

1 INTRODUCTION

Urban Air Mobility (UAM) is on the brink of transforming the urban transportation industry by unveiling modern electric vertical take-off and landing (eVTOL) aircraft that offer efficient, quiet and environmentally sustainable air taxi services. These aircraft also enhance emergency response capabilities by providing rapid deployment for disaster response and medical services, significantly reducing traffic congestion and travel time. Integration of Distributed Electric Propulsion systems with articulated tilting mechanisms lies at the heart of this transformation. The operational versatility of these eVTOLs is demonstrated by their capability to transition from vertical take-off/landing to forward flight and vice versa. This feature has been exemplified by state-of-the-art designs like Vertical Aerospace VX4, Joby S4, and Archer Midnight. The configurational novelty of these aircraft is accompanied by challenging dynamics arising due to rotor-structure and rotor-rotor interactions. The complexity arising from these interactions significantly affects the vibrational behaviour and dynamic stability of the system. This necessitates the development of specialised experiments to help to untangle the dynamic interplay implicit to these eVTOL designs.

To facilitate a controlled investigation into these dynamic interactions arising from the tilting DEP and eVTOL configurations, the experimental rig is proposed in this work aims to emulate these dynamic characteristics. Development and use of dynamically scaled experimental test rigs have played a crucial role in investigating aeroelastic and aerodynamic phenomena that are challenging to study numerically and analytically. Such experimental setups facilitate the exploration of nuanced aeroelastic interactions under controlled conditions [1, 2]. This empirical approach is vital for validating computational models, particularly for innovative aircraft

designs where predicting dynamic behaviour involves complex, nonlinear interactions [3, 4]. Thus, appropriately scaled test rigs play an essential role in bridging the gap between real-world behaviour and numerical simulations, ensuring that emerging novel configurations are safe and viable for future applications [5, 6].

Traditional methods of similitude analysis utilising Reynolds, Froude, Frequency or Strouhal number similarity have been important to aerodynamics and aeroelastic research but, are limited in their ability to completely account for all phenomena of interest, especially in the modern eVTOL structures. Rooted in dimensional analysis, these traditional methods have contributed to significant progress in exploring fluid-structure interaction and resulting dynamic characteristics. However, their applicability is often confined to scenarios that are characterised by a narrow focus and do not account for the broad range of dynamics phenomena in complex systems [7, 8]. With the increase in complexity of aerospace technologies and design configurations, there is a necessity to adopt alternative scaling approach that targets the range of interactions and working conditions to facilitate future innovative research [9–11].

This study introduces an alternative scaling methodology to develop a comprehensive tilting multirotor test rig. The objective behind the development of this scaling method and the tilting multirotor system is to facilitate a systematic investigation of the impact of operational parameters such as tilt angles and rotor speeds on the complex dynamic interactions between the rotor and wing structure. The focus on achieving a measure of dynamic similarity is to promote applicability of the findings to realistic eVTOL configurations and provide an essential understanding of their possible impact on the dynamic and stability characteristics.

To achieve the final rig design, a global optimization algorithm was coupled with a Finite Element (FE) model to calibrate the design parameters of the rig to ensure the proposed measure of dynamic similarity with Maxwell X-57 aircraft. This aircraft was chosen as the baseline model due to its relatively well-defined status in open literature and sufficient relevance to the current DEP and eVTOL technologies. Despite Maxwell X-57's inability to tilt the rotors, it still offers a solid foundation for exploring sensitivity of the dynamic characteristics and vibration responses to the rotor configurational variations. Through this careful alignment with the X-57, the research endeavours to bridge the gap between theoretical modelling and empirical validation, ensuring that the experimental rig not only simulates the relevant dynamics but also, in the medium term, contributes to the broader understanding of their behaviour in transitional flight phases.

This paper is organisd as follow: Section 2 describes the metholdogy for scaling, optimisation, numerical modelling and experimental setup. Section 3 introduces final design of the Bristol Multirotor test rig, validation with NASTRAN simulation and results of experimental exploration. This is followed by conclusions in Section 4.

2 METHODOLOGY

2.1 Overview of Experimental Test Rig

The experimental rig shown in Figure 1 was proposed to facilitate an understanding of the changes in the modal characteristics of tilting rotor systems under controlled parametric variations. Drawing inspiration from the Maxwell X-57's distributed electric propulsion architecture and to optimize the strength-to-weight ratio, this rig employs a main spar realised as a solid aluminium beam with a machined H-shaped cross-section. The main spar is coupled with three

rotor assemblies, each comprising of a brushless electric motor (MN2806 KV400) and a composite propeller (3-bladed 10-inch diameter, 5-inch pitch adopted in the present study). Each motor is connected to the main spar through a hollow rectangular arm, which itself incorporates a clamping mechanism to facilitate easy positional adjustment of the rotors along the length of the beam. The motor is connected to the arm using a tilting hinge to facilitate a manual adjustment of the rotor tilt angle.

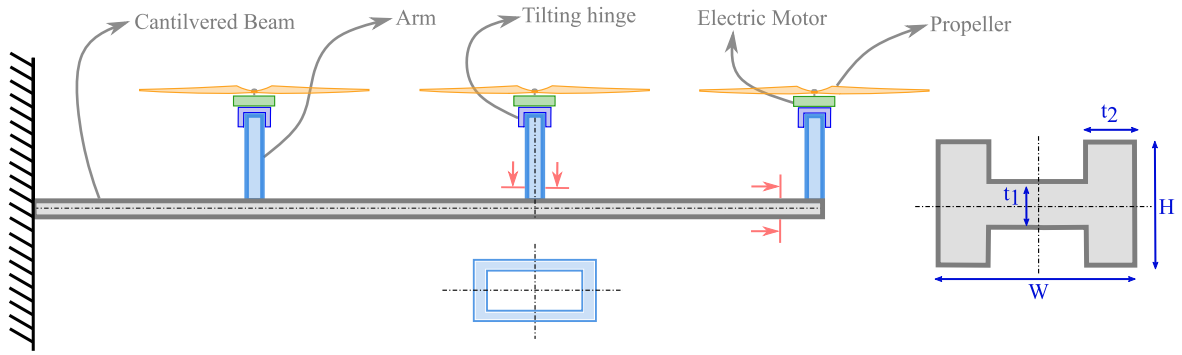

Figure 1: Conceptual sketch of proposed Bristol Multirotor Test Rig

A particular aspect of the rig's functionality is its tilting hinge, designed to replicate the operational versatility of contemporary eVTOL aircraft. This feature permits detailed exploration of variations in the rotor tilt angles and operational speeds, assessing their impact on the key modal parameters such as natural frequencies, mode shapes, and damping characteristics. A detailed optimisation study incorporating a low fidelity beam-based FE model guided the design process.

Table 1: Natural frequencies and frequency ratios of NASA X-57 Maxwell [12]

Modes	**Frequency [Hz]**	**Ratio**
1st Out-of-Plane	2.18	1.00
1st In-Plane	7.09	3.25
2nd Out-of-Plane	13.91	6.38
1st Torsion	16.77	7.69

The FE model discussed in the following sections was coupled with an optimisation algorithm which played an essential role in identifying the optimal dimensions of the rig to emulate the composition of the dynamic characteristics of Maxwell X-57. The aim is to set a solid foundation for future systematic experimental exploration into the complex dynamic behaviour such as resonance, modal interactions and tuning, rotor-structure and rotor-rotor coupling, transient and steady-state nonlinear phenomena, etc.

2.2 Numerical Modeling

For the purposes of initial numerical modelling and optimal sizing, the cantilevered beam spar is modelled using the Euler-Bernoulli beam theory within the bounds of linear elasticity and small deformations. This method is sufficient to simulate the vibration response of the beam and extract its modal characteristics. The rotor assembly and propeller are modelled as point masses for simplicity. This ensures that the complexity of the sizing analysis is maintained

within limits while preserving the essential dynamics that arises when these components are coupled with the beam spar.

Neglecting the axial mobility of the system, each beam FE node within the system is characterized by five degrees of freedom which include the two transversal (bending) deflections and three rotations arising from the beam's bending and torsion. Direct implementation of the rigid rotational transformation matrices facilitates the integration of the rotors' inertial properties to the FE matrices. This approach effectively introduces a rigid link between the point mass and the corresponding beam's FE node and, hence, it ignores the arms' flexibility.

2.2.1 Modelling the beam spar

The solid beam spar is discretised into beam finite elements, where each element is characterised by its stiffness and mass matrix. These are then assembled to form the global stiffness K_{global} and mass matrices M_{global} of the system. The Euler-Bernoulli beam theory is adopted to form the element stiffness matrix, k_{e} which depends on parameter EI, where E represents the Young's modulus and I is the sectional moment of inertia. Meanwhile, the mass matrix, m_{e} depends on the beam's density ρ and cross-sectional area A. The lumped motor-rotor inertial characteristics are added to the global mass matrix using the outlined transformation approach.

The beam's cross-section is modelled as an H-shaped profile, a choice driven by its tuning potential and the structural efficiency it offers in terms of stiffness and weight. The beam's cross-sectional area A, the sectional moments of inertia I_{yy} and I_{zz} about the principal axes, the torsional constant J are computed using the dimensions of the section's flanges and the web. These cross-sectional properties (Equation 1) are used to define the local stiffness and mass matrices for each beam element. Using an appropriate simplification (e.g., neglected sectional fillets, radii, idealised sectional shear flow), the parameters are calculated as follows:

$$\begin{aligned} A &= 2bt + (H-2t)t, \quad I_{yy} = \frac{1}{12}bt^3 + 2\left(\frac{1}{12}t(H-2t)^3\right), \\ I_{zz} &= 2\left(\frac{1}{12}b^3t\right) + \left(\frac{1}{12}t^3(H-2t)\right), \quad J = \frac{1}{3}2bt^3 + \frac{1}{3}t(H-2t)^3 \end{aligned} \tag{1}$$

The element stiffness matrix k_{e}, computed using the cross-sectional properties from Equation 1 sourced from [13], is defined as follows :

$$k_e = \frac{1}{l_e^3}\begin{bmatrix} \frac{12EI_z}{l_e^3} & 0 & 0 & -\frac{12EI_z}{l_e^3} & 0 & 0 \\ 0 & \frac{12EI_y}{l_e^3} & 0 & 0 & -\frac{12EI_y}{l_e^3} & 0 \\ 0 & 0 & \frac{GJ}{l_e} & 0 & 0 & -\frac{GJ}{l_e} \\ -\frac{12EI_z}{l_e^3} & 0 & 0 & \frac{12EI_z}{l_e^3} & 0 & 0 \\ 0 & -\frac{12EI_y}{l_e^3} & 0 & 0 & \frac{12EI_y}{l_e^3} & 0 \\ 0 & 0 & -\frac{GJ}{l_e} & 0 & 0 & \frac{GJ}{l_e} \end{bmatrix} \tag{2}$$

Similarly, the element mass matrix m_{e} can be formulated using the cross-sectional properties

from Equations 1 sourced from [13] in the following form :

$$m_e = \frac{\rho A l_e}{420} \begin{bmatrix} 156 & 0 & 0 & 22l_e & 0 & 0 \\ 0 & 156 & 0 & 0 & 22l_e & 0 \\ 0 & 0 & 4J_p & 0 & 0 & 6J_p \\ 22l_e & 0 & 0 & 4l_e^2 & 0 & 0 \\ 0 & 22l_e & 0 & 0 & 4l_e^2 & 0 \\ 0 & 0 & 6J_p & 0 & 0 & 3J_p \end{bmatrix} \tag{3}$$

The global matrices K_{global} and M_{global} are assembled using the element matrices presented above by mapping the local degrees of freedom (DOFs) of each element to the global system's DOFs, ensuring thus element connectivity and enabing applicaiton of the boundary conditions.

2.2.2 Modelling the rotor arms

The modelling process of the arms connecting the rotors to the main beam involves primarily geometric and mass characterization. The arms are modelled as hollow rectangular links, with their dimensions (width w, height h, and thickness t) defining the cross-sectional area A_{arm} and mass m_{arm}:

$$A_{\text{arm}} = (w \cdot h) - (w - 2t) \cdot (h - 2t) \qquad m_{\text{arm}} = \rho \cdot A_{\text{arm}} \cdot L_{\text{arm}} \tag{4}$$

ρ denotes the material density, and L_{arm} represents the length of the arm.

The contribution of each arm is represented through an incremental mass ΔM_{arm} matrix, derived from the arm's geometry and material properties, which represents the equivalent inertial contribution of this component. This matrix is then incorporated into the global mass matrix M_{global} at the positions corresponding to the nodes where the arms attach to the beam spar. For the purposes of this modelling, the arm is assumed rigid and the corresponding behavior is achieved by the multi-point constraint approach realised using the components' penalty stiffness contributions.

2.2.3 Modelling the rotor assembly

Each non-rotating rotor is modelled as an appropriately positioned point mass. This approach simplifies the rotor dynamics while capturing the essential global inertial effects of the rotor on the system's dynamic behaviour. For each rotor, the model incorporates the mass, the location along the beam (spanwise location), and the offset from the beam's neutral axis. The mass of each rotor m_{rotor} includes the combined weight of the rotor holder, propeller, and motor. The spanwise location x_{rotor} and the transversal offset $(y_{\text{rotor}}, z_{\text{rotor}})$, which accounts for the distance from the beam's neutral axis, influence the rotor's effect on the bending and torsional dynamics.

Similar to the rotor arms, the integration of the rotors into the numerical model is achieved by updating the global matrices. For each rotor, an incremental mass matrix ΔM_{rotor} is calculated based on the rotor's mass and its position along the beam. This incremental mass matrix accounts for both the translational and rotational inertia effects. The rigid offsets from the beam's neutral axis are achieved using the same approach as in the case of the rotor arms.

2.3 Design Optimization

The design of the experimental rig was attained through the integration of the numerical model with a nonlinear optimization algorithm. Adopting this strategy, the numerical model was tuned

to ensure the required aspects of the dynamic similarity with the Maxwell X-57. Dynamic similarity was pursued by establishing a particular composition of the modal properties in the model. Specifically, the model was tuned to align the mode ordering and the ratios of the natural frequencies to the fundamental mode with those reported for Maxwell X-57. Data provided in [12] were used as the reference. This approach ensured that the experimental rig matched the dynamic behaviour of the reference system, facilitating meaningful comparative analysis and validation.

The optimization framework was structured around a nonlinear optimization algorithm employing the Sequential Quadratic Programming (SQP). This algorithm was selected for its efficacy in handling nonlinear objective functions and constraints. The SQP implementation in Matlab's function *fmincon* [14], combined with multiple restarts, was used to reach the optimum parameter configuration. The optimization was facilitated by defining the following objective function

$$J(\mathbf{p}) = \sum_{j=2}^{N_f} \left(\frac{f_{FE,j}}{f_{FE,1}} - \frac{f_{x57,j}}{f_{x57,1}} \right)^2 \quad where \quad \mathbf{p}_L \leq \mathbf{p} \leq \mathbf{p}_U \tag{5}$$

where $\mathbf{p}$ is the parameter vector of the design variables with its lower and upper values $\mathbf{p}_L$ and $\mathbf{p}_U$, respectively, characterising an acceptable design range. In Equation 5, $\frac{f_{FE,j}}{f_{FE,1}}$ refer to the achieved frequency ratio from the eigenvalue analysis and $\frac{f_{x57,j}}{f_{x57,1}}$ refers to the targeted frequency ratio of that corresponding mode. The parameter vector of design variables includes the cross-sectional dimensions of the beam W, H, t_1 and t_2 as shown in Figure 1, which directly influence the beam's modal characteristics.

Hence, the objective function $J(\mathbf{p})$ was used to minimize the difference between the FE natural frequencies and those corresponding to the Maxwell X-57 aircraft, summarised in Table 1 and sourced from [12], while each set was normalised relative to its own fundamental natural frequency. This normalisation strategy was adopted to specifically achieve the matched frequency distributions between the two sets whilst referencing each set to its own first natural frequency. In this way, the frequency $f_{FE,1}$ could be chosen independently and subjected to other considerations such as the nominal motor characteristics (e.g., speed range) or differing criteria arsing from another discipline (e.g., quasi-static structural deflections, root stresses/strains). Further, to ensure the correct ordering of the mode shapes the additional consideration for the desired sequence of the 'out-of-plane', 'in-plane', and 'torsional' modes was applied using equality constraints as shown in Equation 6.

$$\text{ceq}[i] = \begin{cases} 0 & \text{, if Mode}_{\text{FE}}[i] = \text{Mode}_{\text{x57}}[i] \\ 1 \times 10^2 & \text{, if Mode}_{\text{FE}}[i] \neq \text{Mode}_{\text{x57}}[i] \end{cases} \tag{6}$$

Inequality constraints were defined to enforce the physical and experimental feasibility, including geometric constraints on the beam's dimensions. This was done to ensure an H-shaped cross-section by introducing specific geometric relationships and minimum dimensions as shown in Equation 7. An additional inequality constraint was introduced to ensure that a specified targetted mode does not exceed the targetted frequency. This was done to ensure that the frequency of the fourth mode ('torsional') lies within the operational RPM range of the motor.

$$
\begin{aligned}
W - 2t_1 &\geq Flange\ gap \\
H - 2t_2 &\geq Web\ gap \\
t_1 &\geq t_{1\,\min} \\
t_2 &\geq t_{2\,\min} \\
H &\geq W \\
f_{\mathrm{i}} &\geq f_{\mathrm{Target}}
\end{aligned}
\tag{7}
$$

The design variables spanned a feasible design space, defined by the lower and upper bounds based on the preliminary analyses and physical constraints of the experimental setup. To compute the natural frequencies and associated mode shapes for each set of design variables, the FE model described in Section 2.2 was incorporated within the optimization loop. As explained previously, this model accounted for the beam's material properties, cross-sectional geometry, and boundary conditions reflective of the experimental rig's setup. Importantly, the addition of the rotor, arm, etc. introduced localized inertia which significantly affected the modal characteristics. The constraints, in particular, were critical in ensuring that the optimized design not only met the desired natural frequency ratios but also adhered to the practical experimental design limitations.

2.4 NASTRAN FE Model

Following the established design process, after obtaining the optimised dimensions of the proposed test rig, a detailed CAD model was produced using Autodesk Inventor. The CAD model incorporated all the necessary components of the rig including the main spar, arms and rotor assemblies. Subsequent assessment of the CAD design was performed using a high fidelity FE representation in NASTRAN mainly to ensure that the overall system design met the originally targeted dynamic characteristics before the manufacturing and assembly stages of the experimental rig.

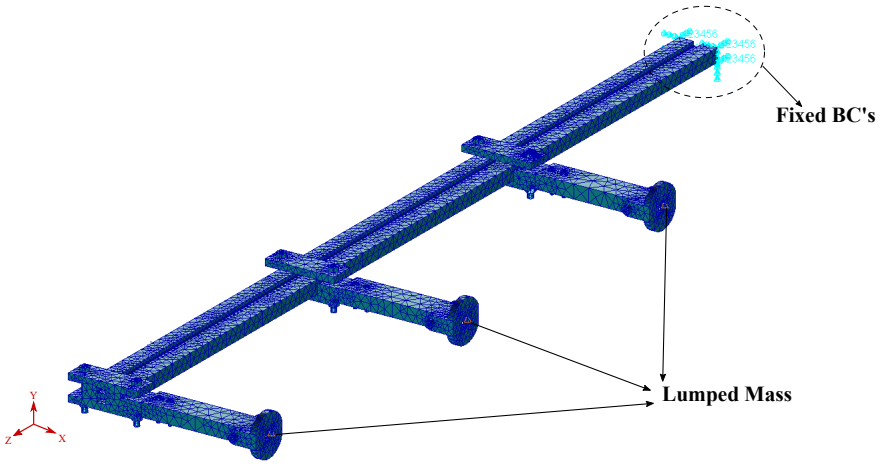

Figure 2: NASTRAN Assembly of the Multirotor Test Rig.

The CAD assembly was imported to the PATRAN workspace as an Initial Graphics Exchange Specification (IGES) file with the correct model units (mm). The IGES imported into the PATRAN workspace included a beam, arm, clamping mechanism and tilting hinge. The motor and propeller were modelled as lumped masses at the centre of gravity of the tilting hinge as

shown in Figure 2. This is followed by the application of appropriate boundary conditions to the assembly. The root of the main spar was fixed to ensure the cantilevered boundary conditions by constraining all the translational and rotational degrees of freedom. Additionally, the constraints were applied to ensure the rigid connection between individual parts such as the rotor assembly and spar.

This is followed by meshing the 3D volume of the assembly using *Tet10* tetrahedral elements. The global edge length was chosen to be 0.1 resulting in 125,316 nodes and 375,948 degrees of freedom. These *Tet10* elements facilitate accurate modelling and meshing of the complex geometries like that of tilting hinges by ensuring better interpolation of displacement and stress fields which is critical for eigenvalue analysis. Material properties of aluminium were applied to the assembly with Young's modulus E of 70 GPa and a density ρ of 2,700 kg/m^3. Finally, eigenvalue analysis was performed over the meshed model using NASTRAN to determine the natural frequencies and mode she shapes of the rig.

2.5 Experimental setup and methods

Figure 3 demonstrates a detailed description of the experimental setup. The experimental setup includes an H-shaped aluminium beam, fixed to a steel clamping pod to ensure rigid boundary conditions. The clamping pod rests on a large, heavy metal block to provide a rigid and stable foundation, ensuring that the structure does not move while experimenting. Two propellers and electric brushless motors (MN2806, KV400) are shown to be connected to the main spar using hollow rectangular tubes, serving as arms. Each propeller has 3 blades with a diameter of 10 inches (=25.4 cm) and a pitch of 3 inches (=12.7 cm). The motor is connected to the arm using an aluminium tilting adaptor, that allows the motor to be locked at a desired tilt angle relative to the arm. A specialised control unit was developed to control the propeller speeds. The control unit is composed of a *teensy 4.1* microcontroller, two 10-watt potentiometers and two 40A ESCs.

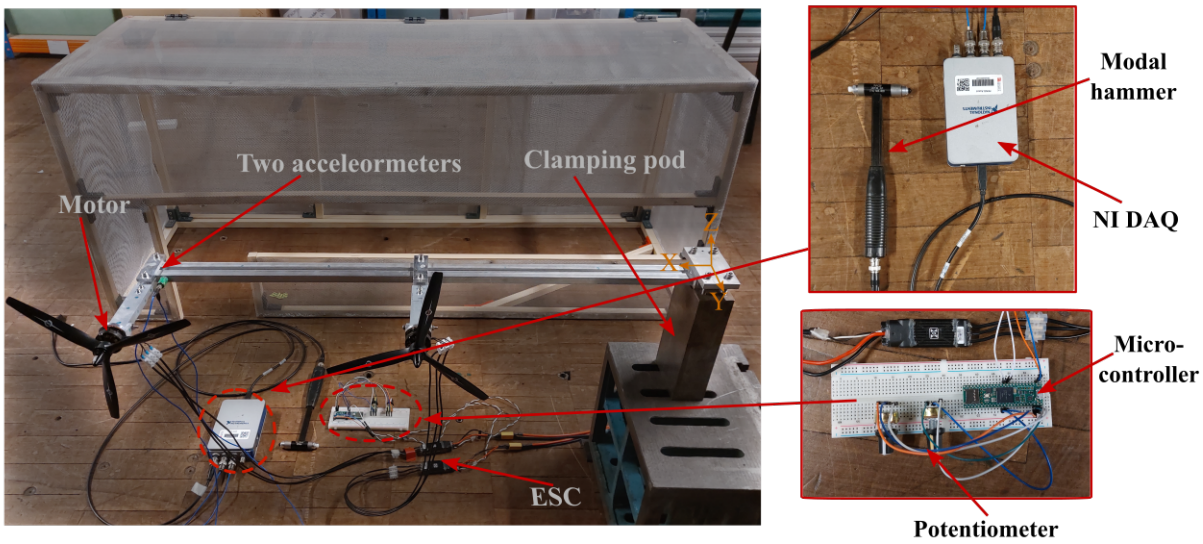

Figure 3: Experimental set-up

Experimental modal analysis (EMA) was performed in the rotating and non-rotating states of the propeller to find the modal properties of the system. The rig is excited at different locations using a modal hammer (PCB 086C03) in X-Y and X-Z planes. Out-of-plane and in-plane

acceleration responses were measured by two PCB 352A25 uni-axial accelerometers. Data acquisition was managed with an NI9234 module, and modal properties were extracted through the *PolyMAX* method from the frequency response functions (FRFs) between the hammer force and accelerations [15]. The modal tests were performed at several rotation speeds of the motor in the range of 0-4550 RPM. Further, transient analysis was conducted by recording the accelerometer response when the rotor speeds are varied within the operational range. The rotor speed gradually increases from 0 to 4550 RPM, holds constant for 5 secs at the peak RPM, and then reduces back to 0.

3 RESULTS

3.1 Optimally Dynamically Tuned Design and Validation

The optimisation process outlined in Section 2.3 resulted in determining the cross-sectional dimensions of the H-beam that reached the targeted frequency ratios and mode shape ordering as listed in Table 1. The optimally tuned dimensions of the H-beam cross-section are summarised in Table 2. The parameters listed in this table also include cross-sectional material properties of the beam, arm and rotor assembly. Based on these parameters, a CAD model of the experimental rig was implemented as shown in Figure 4. Preliminary validation of the reached design was performed in NASTRAN to ensure that the overall system design met the targeted dynamic characteristics. This step served as a comprehensive check to detect any potential discrepancy that could arise in the final implementation after the manufacturing and assembly of the experimental rig.

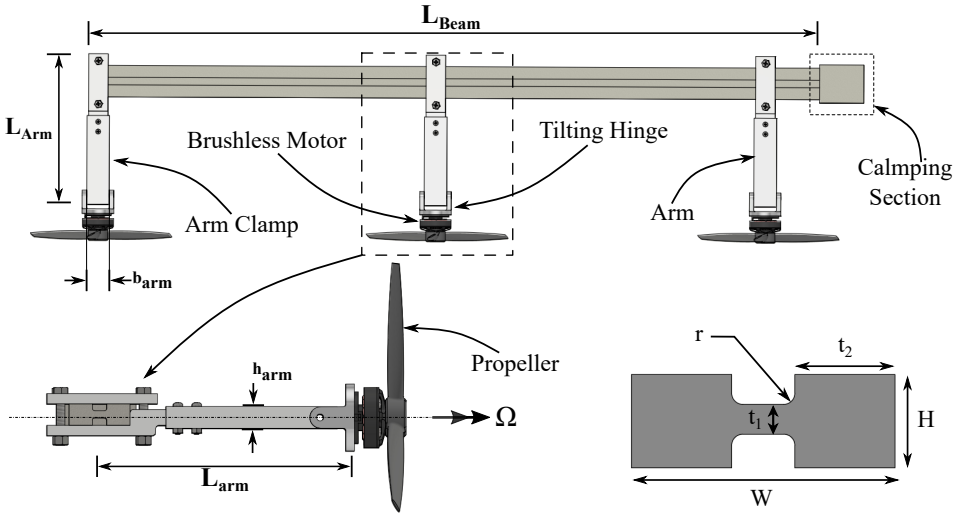

Figure 4: 3D CAD realisation of the Bristol Multirotor Test Rig Assembly.

Table 2: The parameters of the rotor rig model.

Parameter	Value	Parameter	Value
W	3.55×10^{-2} m	b_{arm}	2.50×10^{-2} m
H	1.25×10^{-2} m	h_{arm}	1.25×10^{-2} m
t_1	4.00^{-3} m	t_{arm}	1.50^{-3} m
t_2	1.35^{-2} m	m_{arm}	3.00^{-1} m
m_e	1.00 kg.m^{-1}	L_{arm}	1.35^{-1} m
L_{beam}	8.25^{-1} m	I_{pxo}/I_{pyo}	4.20^{-5} kgm^2
I1	4.46×10^{-9} m^4	m_p	1.20^{-2} kg/m
I2	4.62×10^{-8} m^4	N_b	3
g	9.81 ms^{-2}	ma	8.00^{-2} kg
E	70.00 GPa		

Initial preview of the test rig's dynamics in the frequency domain is demonstrated with the help of the experimental Frequency Response Function (FRF) shown in Figure 5. The configuration used for obtaining this FRF included 3 rotor-arm assemblies at 0° tilt angle in non-rotating condition as shown in Figure 6. A detailed comparison of the natural frequencies and modal orders obtained from optimisation step, NASTRAN simulation and experimental modal analysis is presented in Table 3.

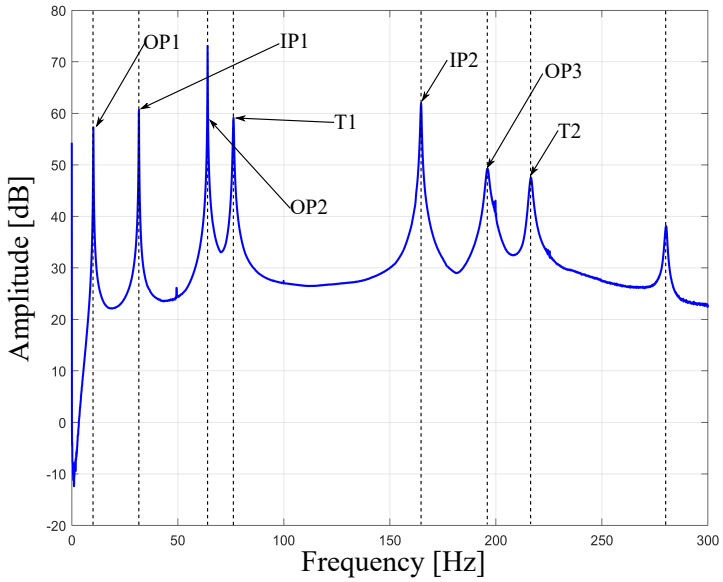

Figure 5: FRF of multirotor test rig with 3 rotor assemblies at 0° tilt angle for non-rotating case.

The frequency of the first bending mode from the NASTRAN model (10.38 Hz) shows a 0.67% deviation from the targeted frequency of 10.45 Hz. In comparison, the frequency from the experimental results (10.23 Hz) shows a deviation of 2.13%. The first in-plane frequency (32.92 Hz) from the NASTRAN simulation results in a 2.49% deviation, while the experimental frequency shows a closer agreement with only a 1.43% deviation from the targeted frequency of 32.11 Hz. The first torsional frequency from the NASTRAN model (70.32 Hz) shows the highest deviation of 11.10% from the optimised frequency (78.58 Hz). On the other hand, the first torsional frequency from experimental results shows a 3.06% deviation. The second bending frequency from NASTRAN (63.36 Hz) and experimental results (64.07 Hz) deviate from the

optimised frequency by 0.76% and 1.87% respectively.

Table 3: Natural frequencies of the multirotor test rig

Mode	Optimisation	NASTRAN	Experiment	
	[Hz]	[Hz]	[Hz]	Damping (%)
1st Bending	10.45	10.38 (0.67%)	10.23 (2.13%)	0.60
1st In-Plane	32.11	32.92 (2.49%)	31.66 (1.43%)	0.26
2nd Bending	62.88	63.36 (0.76%)	64.07 (1.87%)	0.07
1st Torsion	78.58	70.32 (11.10%)	76.21 (3.06%)	0.25

Finally, the mode shapes of the targeted modes are compared in Figure 6. It can be observed that the order of the modes achieved is retained across all three methods, namely first out-of-plane, first in-plane, second out-of-plane and first torsion. This confirms the reliability of the optimisation process.

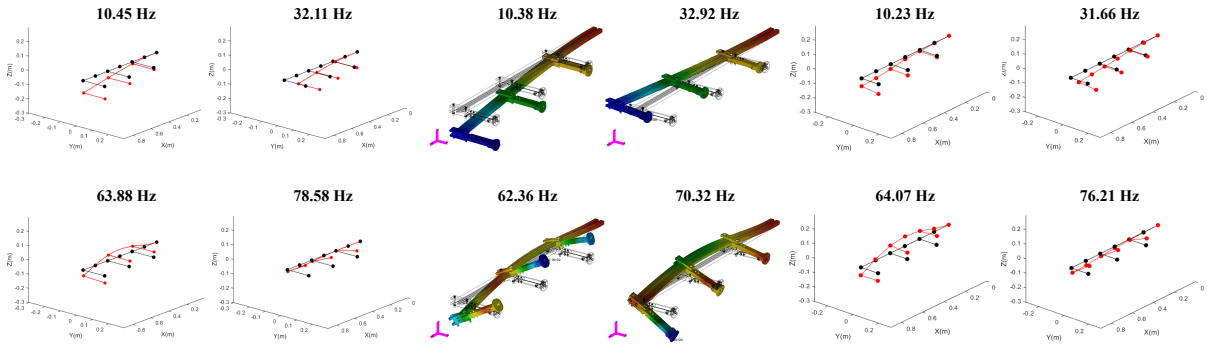

(a) MATLAB FEA Model (b) NASTRAN Model (c) Experiment Modal Analysis

Figure 6: Summary comparison of the computational and experiment modal analysis results.

Damping ratios from experiment modal analysis are also shown in Table 3, giving additional insights into the resonant characteristics of the rig. Overall, the damping ratio levels are well below the 1% mark. The lowest damping ratio of 0.07% is observed for the second bending mode, indicating notably limited energy dissipation and the possibility of strong resonant events. Such low values of damping ratios are undesirable for real-life applications. However, in this case, low damping ratios are advantageous from an experimental point of view to witness and explore the targeted dynamic phenomena.

3.2 Experimental Exploration

3.2.1 Time-domain Analysis

Time-domain analysis provides useful insights into how the dynamic characteristics of the tested system change when the operational conditions are varied. For the given case of a single propeller and arm attached to the tip of the beam, time domain analysis was conducted by increasing the propeller speed gradually from 0 to 4550 RPM, holding it constant at 4550 RPM and then gradually reducing it back to 0 RPM. This configuration with single arm and propeller assembly attached at the beam tip would be used for experimental exploration in section ahead.The RPM was varied manually by gradually turning the potentiometer knob. Out-of-plane and in-plane

accelerometer data were recorded for the entire duration of the test and plotted as shown in Figure 7.

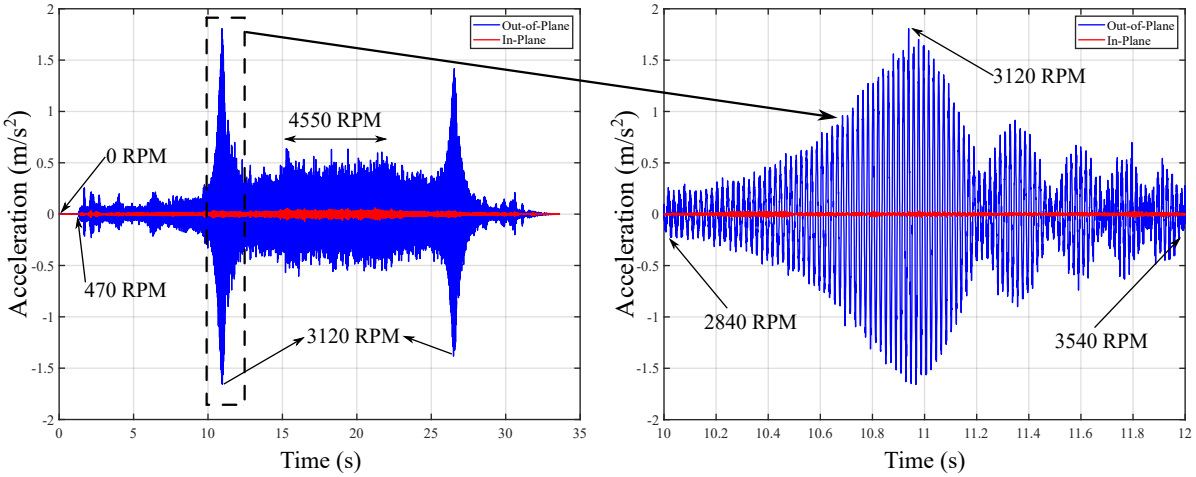

Figure 7: Time vs acceleration plot for the out-of-plane and in-plane accelerometers when the rotor RPM is varied from 0-4550, held constant and then reduced from 4550-0 RPM.

At the start (0-1 seconds), the rotor speed is at 0 RPM, and no physical acceleration is observed in both the out-of-plane and in-plane directions. This serves as a baseline by establishing the quiescent state of the test rig. From 1-16 seconds, the rotor RPM is increased gradually from 465-4550 RPM. The minimum RPM at which the motor starts spinning is 465 RPM. This is because the Electronic Speed Controller (ESC) has a threshold voltage below which the motor does not have enough power to overcome the internal friction and resistance. The amplitude of acceleration recorded for both out-of-plane and in-plane directions increases noticeably. However, the increase in out-of-plane acceleration is more profound. This indicates that the primary response of the system is in the out-of-plane direction. This further suggests the dominant participation of the out-of-plane bending modes in response to the unbalance excitation arising from the spinning motor-propeller assembly. As the rotor speed increases from 2840-3120 RPM (10-11 sec.), the out-of-plane acceleration increases significantly, indicating the combined influence of the weakly damped vibration mode under conditions of the resonant excitation. A significant peak is observed at 3120 RPM in the out-of-plane acceleration data. The peak highlights that the system experiences resonance. This is because the rotor speed of 3120 RPM, excites the natural frequency of the second out-of-plane bending mode (52 Hz), which leads to the extreme vibration amplitude.

The rotor speed is then held constant at 4550 RPM from 16-23 sec., which can be observed from the relatively steady acceleration readings as shown in Figure 7. This steady-state response at higher rotor speed shows significantly greater amplitudes compared to regions of lower speeds. This is highlighted by the increased vibration activity and potential resonant interaction of the system with the higher rotor harmonics. Similar effects are observed when the rotor speed is reduced back to 0 RPM. After the 35-second time stamp, the rotor RPM is back to 0 where the system returns to the quiescent state.

3.2.2 Frequency-domain Analysis

Analysing the Frequency Response Function (FRF) plots facilitates a comprehensive understanding of the system's dynamic characteristics across the frequency range. They also facili-

tate contextual understanding of how the characteristics change with a variation in the test rig's configuration.

Figure 8 compares FRFs for different propeller speeds at a 0-degree rotor tilt angle. This figure highlights the distinct resonant peaks corresponding to the first four natural frequencies of the test rig within the frequency range of 0-120 Hz. The figure also presents the detail of the peak corresponding to mode 4 to illustrate its evolution under the rotor speed variations. The FRF's show response from the out-of plane accelerometer, placed under the arm connecting rotor assembly to the main spar as shown in 4.

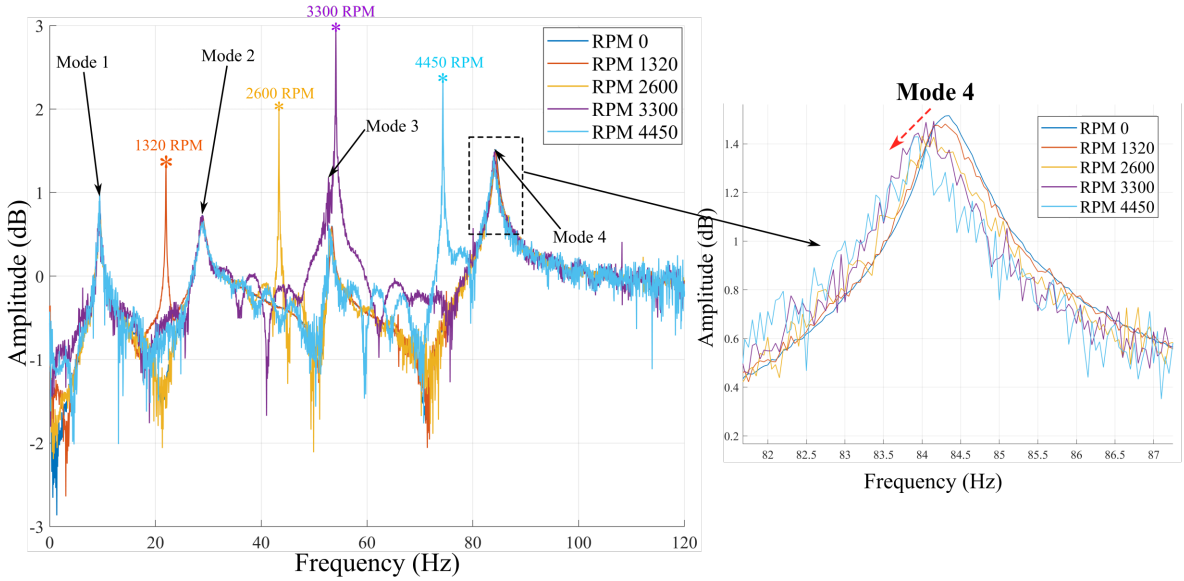

Figure 8: Comparison of the FRFs for the chosen propeller speeds in the range from 0 to 4450 RPM at the 0° tilt angle.

From Figure 8, it can be observed that, with an increase in the rotor speed, the modal peaks are relatively insensitive to this operational change. Closer inspection of these primary features reveals, however, that they undergo minor variations both in terms of the corresponding frequency values and amplitudes. This behaviour is illustrated in case of mode 4 in a separate plot shown in the same figure. Furthermore, apart from the inherent modal properties, owing to their operational nature, these functions contain the narrow band peak artefacts that can be attributed to the steady-state component of the vibration response caused by the spinning propeller. As expected, these non-modal peaks vary their position significantly with the varying rotor speed. In particular, by design, the condition of 3300 RPM manifests the near-resonant characteristics where the rotor excitation almost matches the third natural frequency (OP2).

Figure 8 also indicates that the fourth mode demonstrates a trend where the amplitude and frequency reduces with increasing rotor speed. To enable a closer inspection of this trend, the representative modal feature in the form of the peak frequency and amplitude were identified across all considered rotor speed cases and are summarised in Figure 9

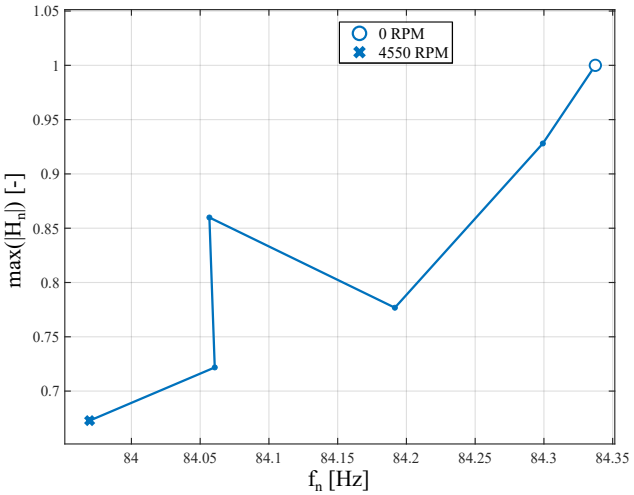

Figure 9: Change in the peak characteristics of Mode 4 at 0° with the varying rotor speed.

It can be seen that the mode 4 peak characteristics associated with the natural frequency and modal damping, display tendency to decrease concurrently and monotonously. However, a notable exception from this trend is observed for the case of 3300 RPM case where the peak amplitude rapidly rises whilst the frequency disproportionately drops. The subsequent case of 3910 RPM suggests return to the overall gradual trend. The outlined deviation from this trend is attributed to the near-resonant conditions which are, however, experienced due to interaction of the first rotor harmonics and mode 3. In that sense, this behaviour can be seen as a manifestation of nonlinear coupling and energy redistribution between the underlying vibration modes of the real system.

To complement the previous parametric study, Figure 10 shows FRFs for the different rotor tilt angles at a constant speed of 3300 RPM. In this case, a constant rotor speed was chosen strategically to help to understand how these characteristics change with the tilt angle variation when positioning the rotor speed close to one of the natural frequencies while, at the same time, ensuring the integrity and safety of the tested system.

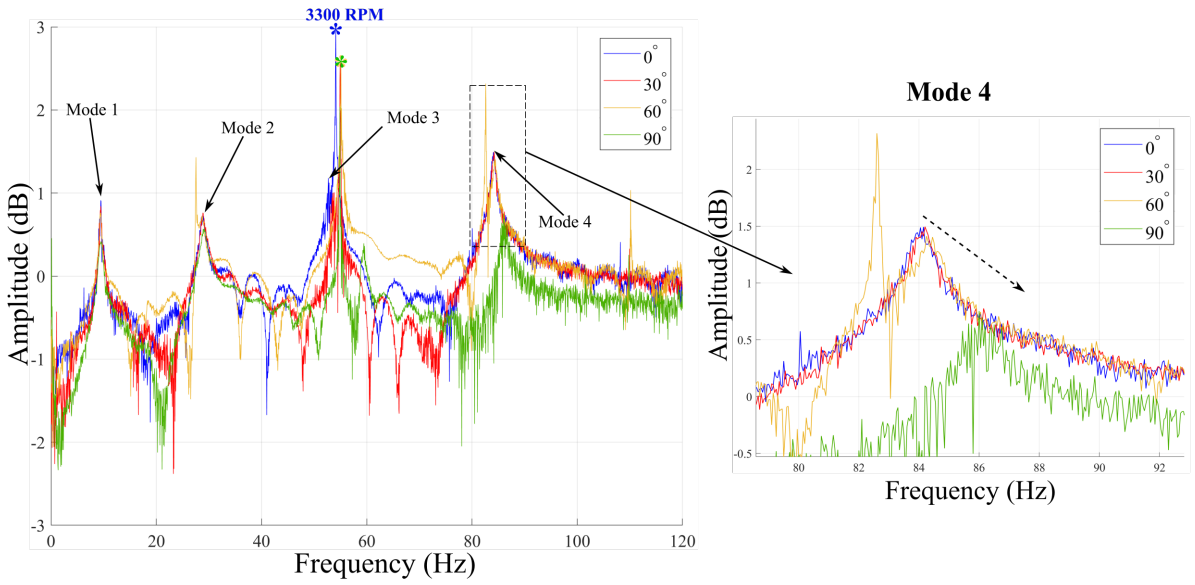

Figure 10: Comparison of the FRFs for different propeller tilt angles (0-90°) at 3300 RPM.

It can be seen that the amplitudes of the modal peaks reduce consistently when tilt angles are increased from 0-90°. This reduction in amplitude is most at higher tilt angles, particularly at 90° cases where the rotor is in vertical take-off/landing configuration. The reduction in the amplitudes is accompanied by a change in the frequency. The frequency of the first out-of-plane bending mode reduces marginally by 0.52% when the rotor tilt angle is increased from 0 to 90°. Whereas, the natural frequencies increase significantly for higher modes with an increase in tilt angles.

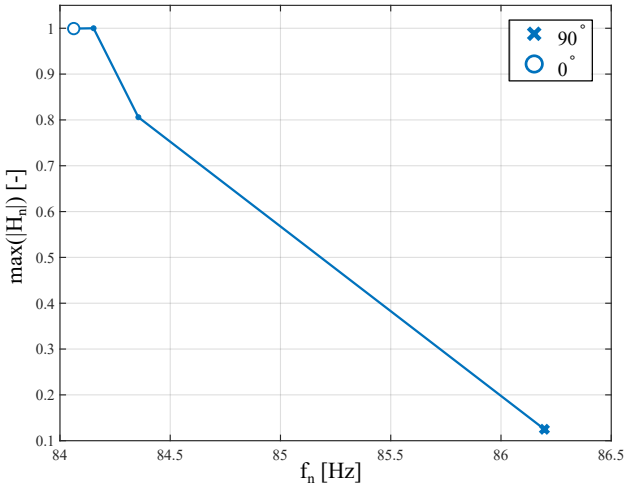

Figure 11: Change in the peak characteristics of Mode 4 at 3300 RPM° with the varying rotor tilt angles.

It can be seen, in this targeted feature analysis, that mode 4 is significantly impacted by the applied configurational variation represented by the tilt angle. The dominant and monotonous and near-linear trend in the identified frequency and peak values suggests the decrease of the amplitudes whilst the natural frequencies increase substantially. On the one hand, the frequency increase is likely to be mainly caused by the geometric reconfiguration of the rig where the centre of mass of the motor-rotor assembly moves closer to the beam's neutral axis decreasing, hence, its effective rotational inertia relative to the beam's elastic axis. On the other hand, the amplitude decrease with increasing tilt angle is thought to be associated with aeroelastic influences. The rotor reorientation toward greater tilt angles produces aerodynamic loading system, at the point of the rotor shaft, which becomes increasingly effective in affecting torsional dynamics of mode 4.

3.2.3 Spectral Analysis

A short-time Fourier transform of the acceleration-time signal shown in Figure 7 was performed using the *spectrogram* function in MATLAB [16]. The resulting spectrogram plot in Figure 12 demonstrates how the composition of the accelerometer signal changes with time and frequency when the rotor speed is increased from 0 to 4550 RPM, held constant and then reduced back to 0 RPM. The strength/amplitude of the acceleration signal is represented using a 'hot' colour scale with lower amplitudes of acceleration shown with dark red colour and higher amplitudes highlighted with yellow colour.

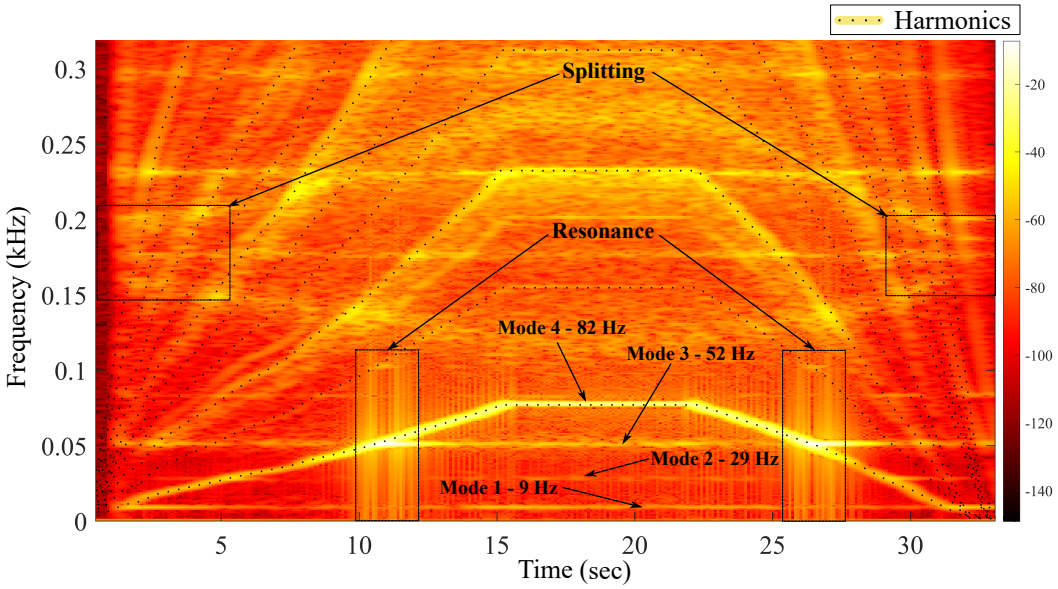

Figure 12: Spectrogram plot at 0° tilt angle when the rotor speed is increased from 0 to 4550 RPM, held constant and decreased back to 0 RPM.

A rich range of features and phenomena can be observed in the figure as a results of significant rotor speed changes. The spectrogram plot clearly highlights distinct harmonic frequencies related to the rotational speed of the rotor. Observing these, it can be seen that the rotational speed was increased from 0 to 4550 RPM (∼76 Hz), held constant at 4550 RPM, and then reduced back to 0 RPM. These rotor harmonics were detected and plotted computationally using the corresponding Power Spectral Density (PSD) information in an automated manner. Further, the natural frequencies of the first 4 modes from the spectrogram plot are observed to be 9, 29, 52 and 78 Hz, respectively, at 4550 RPM. These values complement the natural frequencies observed from the FRF plots in Figure 8.

Further, it can be witnessed that when the rotor harmonics pass the natural frequency of the structure, the acceleration amplitude increases, indicating resonant interactions. The interaction between the vibration modes of the system and the rotor harmonics can be seen on spectrogram plots across multiple distinct time-frequency regions. In particular, the most prominent resonant event occurs at 52 Hz, where the first rotor harmonics interacts with the second out-of-plane bending mode. This particular strong resonance is influenced by relatively low damping levels which (in case of the three-arm configuration) are presented in Table 3. Other less significant resonant phenomena can be observed in case of higher harmonic rotor interactions with the natural frequencies that present themselves as being nearly constant (beam-dominated) as well as those that are notably sensitive (rotor arm-dominated) under the rotor speed variations. It should also be highlighted that the selected frequency range from 0 to 320 Hz features not only the originally studied first four modes but also other modes associated with more complex dynamic rig activity.

A distinctive phenomenon seen in the spectrograms is manifested as the sensitive variation of a pair of the frequencies constituting a mode splitting pattern in the highlighted region of 170-190 Hz. Since the minimum RPM at which the motor starts spinning is 465 RPM, the origin of this behaviour from the non-rotating condition is not observable in the spectrogram. It can be observed that the difference between the split branches increases as the rotational speed of the propeller increases. The branch with the decreasing frequency with the rotor speed is typi-

cally classified as the backward whirl mode, whereas the branch with the increasing frequency is classified as the forward whirl mode. The backward whirl mode features whirling in the opposite direction to the rotor rotation, whereas the forward whirl mode features the whirling in the same direction as the rotor. An additional mode is spotted that appears to coincide with the origin of the splitting but is insensitive to the changes in the rotor speed.

To gain further insight into the associated dynamics, the validated NASTRAN FE model is adopted for a single rotor configuration such that the isolated non-rotating dynamic activity of the arm-rotor-propeller assembly can be assessed. The assembly is isolated from the main spar in the model by constraining all translational and rotational degrees of freedom of the main spar. Figure 13 shows the results of the eigenvalue analysis of this isolated assembly.

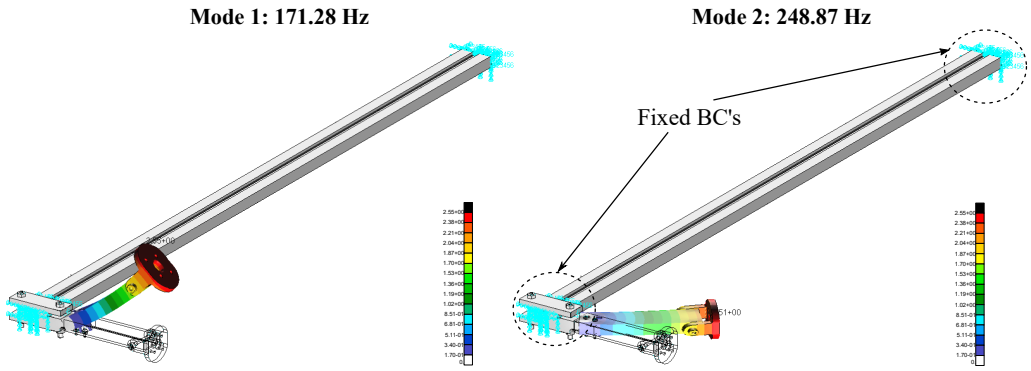

(a) First out-of-plane mode of isolated arm (b) First In-plane mode of isolated arm

Figure 13: Mode shapes of the isolated arm-motor-rotor assembly computed using NASTRAN FE model

.

It can be observed that the first out-of-plane and first in-plane modes of the isolated rotor-arm assembly occur at 171.28 Hz and 248.87 Hz, respectively. Specifically, the frequency of the first out-of-plane bending mode associated with the dominant arm's activity aligns with the corresponding stationary frequency in the spectrogram of the full rig which, additionally, coincides with the origin of the splitting frequency branches. It is noted that all three frequencies encounter resonant conditions with various rotor harmonics throughout the presented test scenario.

4 CONCLUSION

The research involved exploring the impact of rotor speed and tilt angles on the dynamic characteristics and vibrational response using experimental modal analysis. To understand the dynamic interplay between modal characteristics of a tilting multirotor system, a dynamically scaled experimental inspired by NASA Maxwell X-57 is developed. A novel scaling methodology and optimisation have been developed to design the dynamically scaled experimental rig. NASTRAN simulations were used to validate the dynamic characteristics of the design before manufacturing and assembly of the rig. It was observed that the order of the modes achieved is retained across all three methods, namely first out-of-plane, first in-plane, second out-of-plane and first torsion, confirming the reliability of the optimisation process. The experimentally obtained natural frequencies of these first four modes are as follows: 10.23, 31.66, 64.07 and 76.21

Hz. The frequencies obtained experimentally aligned closely with optimised target values and NASTRAN simulation.

Experimental exploration indicated that the rotor speed has a noticeable impact on the system's modal characteristics. Reduction in the natural frequencies particularly at the higher modes was observed as the rotor speed increased due to the gyroscopic forces of the propeller. However, the amplitude of vibration was insensitive to changes in rotor speed. The peak characteristics of the fourth mode demonstrated a tendency to decrease concurrently and monotonously as the rotor speed increased. An irregularity is observed in this trend at the 3300 RPM, due to the near-resonant conditions experienced due to the interaction of the first rotor harmonics and mode 3. Further, the impact of variation in tilt angle on modal characteristics was explored at a constant speed of 3300 RPM. It is observed that all modal frequencies increased with an increase in the tilt angles from 0° to 90°, whereas the amplitudes of the peaks consistently decreased. This characteristic is dominant in mode 4 where a substantial increase in frequency and reduction in amplitude is observed.

It was confirmed from the transient analysis that the system experiences strong resonance at 3120 RPM, where the second out-of-plane bending (52 Hz) is excited by the first rotor harmonics. This particular strong resonance is influenced by relatively low damping levels of the third mode (0.07%). This was evidenced by a spectrogram that highlights regions of resonance clearly, where the rotor harmonics interact with the system's natural frequency. It is noted that all three frequencies encounter resonant conditions with various rotor harmonics. Additionally, the spectrogram demonstrated a splitting-like phenomenon in the frequency range of 170-190 Hz, hinting towards complex rotor-structure interaction.

Further investigation will be focused on the influence of rotor-rotor interaction on the dynamic characteristics of the multirotor test rig due to the presence of an additional rotor.

ACKNOWLEDGEMENT

The authors would like to thank the Engineering and Physical Sciences Research Council (EPSRC) for funding this research project under Grant No. EP/T517872/1. Further thanks are extended to the lab technicians Adrian Kraft and Ricky Billingham, for supporting the lab activities.

5 REFERENCES

[1] Pontillo, A., Hayes, D., Dussart, G., et al. (2018). Flexible high aspect ratio wing: Low cost experimental model and computational framework. In *AIAA Atmospheric Flight Mechanics Conference, AIAA SciTech Forum*. Orlando, Florida. doi:10.2514/6.2018-1014.

[2] Yusuf, S. Y., Hayes, D., Pontillo, A., et al. (2019). Aeroelastic scaling for flexible high aspect ratio wings. In *AIAA Scitech 2019 Forum*. p. 1594.

[3] Wang, G., Zhang, M., Tao, Y., et al. (2020). Research on analytical scaling method and scale effects for subscale flight test of blended wing body civil aircraft. *Aerospace Science and Technology*, 106, 106114.

[4] Banneheka Navaratna, P. D., Pontillo, A., Rezgui, D., et al. (2022). Design and assessment of subscale flexible high aspect ratio cantilever wings. In *AIAA SCITECH 2022 Forum*. p. 1305.

[5] Saltari, F., Pizzoli, M., Gambioli, F., et al. (2022). Sloshing reduced-order model based on neural networks for aeroelastic analyses. *Aerospace Science and Technology*, 127, 107708.

[6] Gu, H., Healy, F., Rezgui, D., et al. (2024). Aeroelastic scaling of a high aspect ratio wing incorporating semi aeroelastic hinge. In *AIAA SCITECH 2024 Forum*. p. 0618.

[7] Jordan, T., Langford, W., and Hill, J. (2005). Airborne subscale transport aircraft research testbed-aircraft model development. In *AIAA Guidance, Navigation, and Control Conference and Exhibit*. p. 6432.

[8] Nguyen, N. T., Ting, E., Chaparro, D., et al. (2017). Multi-objective flight control for drag minimization and load alleviation of high-aspect ratio flexible wing aircraft. In *58th AIAA/ASCE/AHS/ASC Structures, Structural Dynamics, and Materials Conference*. p. 1589.

[9] Birkhoff, G. (1960). Hydrodynamics princeton university press. *Princeton, NJ*.

[10] Ricciardi, A. P., Eger, C. A., Canfield, R. A., et al. (2014). Nonlinear aeroelastic-scaled-model optimization using equivalent static loads. *Journal of Aircraft*, 51(6), 1842–1851.

[11] Ricciardi, A. P., Canfield, R. A., Patil, M. J., et al. (2016). Nonlinear aeroelastic scaled-model design. *Journal of Aircraft*, 53(1), 20–32.

[12] Hoover, C. B., Shen, J., Kreshock, A. R., et al. (2017). Whirl flutter stability and its influence on the design of the distributed electric propeller aircraft x-57. In *17th AIAA Aviation Technology, Integration, and Operations Conference*. p. 3785.

[13] Logan, D. L. (2007). *A First Course in the Finite Element Method*. University of Wisconsin–Platteville: Cengage Learning, fourth ed.

[14] MathWorks (2024). Matlab optimization toolbox: fmincon. Accessed: 2024-02-10.

[15] Herman Van der Auweraer, P. G. and Leurida, J. (2004). The polymax frequency-domain method: A new standard for modal parameter estimation. In *Shock and Vibration 11*. pp. 3394–409.

[16] MathWorks (2024). Spectrogram function documentation. Accessed: 2024-02-10.

COPYRIGHT STATEMENT